Customer	: **ESA/ESRIN**	**Document Ref**	: **TN-WP224-001-ARMINES**
Contract No	: **21125/07/1-OL**	**Issue Date**	: **18 July 2008**
WP No	: **224**	**Issue**	: **0.1**

Title : **Image Quality – WP224**

Abstract : WP224 : Image Quality (ARMINES)

Author : Philippe BLANC,
Lucien WALD

Approval :

Accepted :

Distribution :

Hard Copy File:
Filename: TN-WP224-001-ARMINES-Ed0.1.doc

This Page Is Intentionally Blank

TABLE OF CONTENTS

TABLE OF FIGURES

AMENDMENT POLICY

This document shall be amended by releasing a new edition of the document in its entirety. The Amendment Record Sheet below records the history and issue status of this document.

AMENDMENT RECORD SHEET

ISSUE	DATE	DCI No	REASON
Ed0.1	18 Jul 2008	N/A	Initial Issues

This Page Is Intentionally Blank

1. APPLICABLE AND REFERENCE DOCUMENTS

The following is a list of documents with a direct bearing on the content of this report. Where referenced or applicable in the text, these are identified as RD.n or AD.n, where 'n' is the number in the list below

1.1 Reference Documents

ID document	Document reference
[RD1]	Asmami M., Wald L., 1993. A method for an accurate in-flight calibration of AVHRR data for vegetation index calculation. *In Remote sensing for monitoring the changing environment of Europe*, pp. 53-57. Edited by P. Winkler, A.A. Balkema Publishers, Rotterdam.
[RD2]	Asmami M., Wald L., 1993. Interband calibration of the POLDER sensor. *In Remote sensing for monitoring the changing environment of Europe*, pp. 253-259. Edited by P. Winkler, A.A. Balkema Publishers, Rotterdam.
[RD3]	Biggar, S.F., M. Dinguirard, D. Gellman, P. Henry, R. Jackson, M.S. Moran, P.N. Slater, 1991. Radiometric calibration of SPOT2 HRV - A comparison of three methods, *In Proc. SPIE 1943*, pp. 155-162.
[RD4]	Choi, T., 2003. Generic sensor modeling. *In Proceedings of the 2003 high spatial resolution commercial imagery workshop*, Reston, VA, USA, 19-21 May 2003, NASA/NIMA/USGS Joint Agency Commercial Imagery Evaluation Team.
[RD5]	Cosnefroy, H., M. Leroy and X. Briottet, 1996. *Selection and characterization of Saharan and Arabian desert sites for the calibration of optical satellite sensors*, Remote Sensing of Environment, 58, pp. 101-114.
[RD6]	Curran, P. J., Dungan J. L., 1989. *Estimation of signal-to-noise: A new procedure applied to AVIRIS data*. IEEE Transactions on Geosciences and Remote Sensing, 27(5), pp. 620-628.
[RD7]	Delvit, J.M., D. Léger, S. Roques, C. Valorge. 2003. Estimation de la Fonction de Transfert de Modulation à l'aide d'un réseau de neurones. In: Proceedings of the 2003 GRETSI conference, 3 pp.
[RD8]	Delvit, J.M., D. Léger, S. Roques, C. Valorge. 2003. Modulation Transfer Function and noise assessment. In Proceedings of IEEE International Geoscience and Remote Sensing Symposium, July 2003, Vol. 7, pp. 4500-4502.
[RD9]	Donoho, D.L. and Johnstone, I.M., 1994. *Ideal spatial adaption via wavelet shrinkage*. Biometrica. v80. pp. 425-455.

[RD10]	Govaerts, Y. M., 1999. *Correction of the Meteosat-5 and -6 radiometer solar channel spectral response with the Meteosat-7 sensor spectral characteristics.* Int. J. Remote Sens., 20, pp. 3677-3682.
[RD11]	Govaerts, Y. M., B. Pinty, M. M. Verstraete, and J. Schmetz, 1998. Exploitation of angular signatures to calibrate geostationary satellite solar channels. *In Proc. IGARSS '98 Conf.*, (No. 98CH36174), Seattle, WA, IEEE, 327-329.
[RD12]	Guo, Q., Dou X, 2008. *A modified approach for noise estimation in optical remotely sensed images with a semivariogram: principle, simulation, and application.* IEEE Transactions on Geosciences and Remote Sensing, 46(7), pp. 2050-2060.
[RD13]	Helder, D., 2003. In-flight characterization of the spatial quality of remote sensing imaging systems using point spread function estimation. *In International Workshop on Radiometric and Geometric Calibration*, Gulfport, Mississippi, USA.
[RD14]	Helder, D., T. Choi, M. Rangaswamy. 2004. In-flight characterization of spatial quality using point spread function. *Post-launch Calibration of Satellite Sensors*, Morain & Budge Eds, Taylor & Francis Group, London, UK, ISBN 90 58 09 693 9, pp. 151-170.
[RD15]	Helder, D. L.; Choi, T., 2005. *Generic sensor modeling using pulse method.* NASA Technical Report # 20050214150, 58 pp.
[RD16]	Henry P., Meygret A., 2001. *Calibration of HRVIR and Vegetation cameras on SPOT4.* Adv. Space Res., 28, pp. 49-58.
[RD17]	Jenkins, G.M. and D.G. Watts, 1969. *Spectral Analysis and its Applications.* Holden-Day, San Francisco, 525 pp.
[RD18]	Kubik Ph., Breton E., Meygret A., Cabrières B., Hazane Ph., Léger D., 1998. SPOT4 HRVIR first in-flight image quality results. *In Proceedings of the EUROPTO Conference on Sensors, Systems, and Next-Generation Satellites*, Barcelona, Spain, September 1998, SPIE vol. 3498, pp. 376-389.
[RD19]	Leachtenauer, J. C., Malila, W., Irvine, J. M., Colburn, L. P., Salvaggio, N. L., 1997. General image-quality equation: GIQE. *Applied Optics*, 36(32), pp. 8322-8328.
[RD20]	Lebègue L., Pascal V., Meygret A., Léger D., 2003. SPOT5 radiometric image quality. *In Proceedings of the IGARSS 2003*, pp. 306-308.

[RD21]	Lefèvre M., Bauer O., Iehle A., Wald L., 2000. *An automatic method for the calibration of time-series of Meteosat images.* International Journal of Remote Sensing, 21, 5, pp. 1025-1045*.*
[RD22]	Léger, D., J. Duffaut, F. Robinet. 1994. MTF measurement using spotlight. *In* Proceedings of IEEE Geoscience and Remote Sensing Symposium. Pasadena, CA, U.S., Vol. 4, pp. 2010-2012.
[RD23]	Léger, D., F. Viallefont, P. Deliot. C. Valorge. 2004. On-orbit MTF assessment of satellite cameras. *Post-launch Calibration of Satellite Sensors*, Morain & Budge Eds, Taylor & Francis Group, London, UK, ISBN 90 58 09 693 9, pp. 67-75.
[RD24]	Leloglu, U.M., E. Tunali. 2006. On-orbit modulation transfer function estimation for BilSAT imagers. *In* Proceedings of the ISPRS Congress (Commission I, WG 1/6). Paris, France, July 2006, 7 pp.
[RD25]	Markham B. L., J. R. Irons, D. W. Deering, R. N. Halthore, R. R. Irish, R. D. Jackson, M. S. Moran, S. F. Biggar, D. I. Gellman, B. G. Grant, J. M. Palmer, P. N. Slater, 1990. Radiometric calibration of aircraft and satellite sensors at White Sands, NM. *In Proceedings of the Geoscience and Remote Sensing Symposium*, 1990, pp. 515-518.
[RD26]	Matheron, G., 1963. *Principles of geostatistics*, Economic Geology, 5'8, pp. 1246-1266.
[RD27]	Mugnier, L. M., G. Le Besnerais. 2001. Optical transfer function identification from satellite images. *In* Proceedings of the SPIE's 46th annual meeting "Earth observing systems VI" conference, San Diego, CA, USA, July, vol.4483. pp. 185-195.
[RD28]	Oppenheim, A.V., and R.W. Schafer, 1975. *Digital Signal Processing*. Prenctice-Hall Inc., Englewood Cliffs, New Jersey, 608 pp.
[RD29]	Panchev S., 1971. *Random Functions and Turbulence*. Pergamon Press, 444 pp.
[RD30]	Papoulis, A. 1987. *Signal Analysis (3rd printing)*. McGraw-Hill International Editions, Electrical & Electronic Engineering Series. ISBN 0-07-Y 66468-4.
[RD31]	Paxman, R. G., Schulz T., Fienup J. R., 1992. *Joint estimation of object and aberrations by using phase diversity*. J. Opt. Soc. Am. A, Vol. 9, No. 7.
[RD32]	Porez F., Sylvander S., 2007. *SPOT. Image quality performances*. CNES document #C443-NT-0-296-CN, 35 pp.

[RD33]	Press, W., Teukolsky S., Vetterling W. and Flannery B., 1992. *Numerical Recipes in C*, second edition. Cambridge University Press. 994 pp.
[RD34]	Rigollier C., Lefèvre M., Blanc Ph., Wald L., 2002. *The operational calibration of images taken in the visible channel of the Meteosat-series of satellites*. Journal of Atmospheric and Oceanic Technology, 19(9), pp. 1285-1293.
[RD35]	Sèze, G., and M. Desbois, 1987. *Cloud cover analysis from satellite imagery using spatial and temporal characteristics of the data*. J. Climate Appl. Meteor., 26: 287-303.
[RD36]	Sèze, G., and W.B. Rossow, 1991. *Time-cumulated visible and infrared radiance histograms used as descriptors of surface and cloud variations*. Int. J. Remote Sensing, 12: 877-920.
[RD37]	Stern, A., N.S. Kopeika, 1997. Analytical method to calculate optical transfer functions for image motion and vibrations using moments. *Journal of Opt. Soc. Am.* A. Vol. 14, No. 2. pp. 388-396.
[RD38]	Thomas, C. 2006. Fusion d'images de résolutions spatiales différentes. Ph. D. Thesis, Ecole des Mines de Paris. December 2006. 189 pp.
[RD39]	Thome, K., J. Czapla-Myers, S. Biggar, 2004. Railroad Valley Playa for use in vicarious calibration of large footprint sensors. *In Proc. of the Workshop on Inter-Comparison of Large Scale Optical and Infrared Sensors*, 12-14 October 2004, Noordwijk, The Netherlands, ESA WPP-244, February 2005, European Space Agency.
[RD40]	Vermote E. and Y.J. Kaufman, 1995. *Absolute calibration of AVHRR visible and near infrared channels using the ocean and cloud views*, International Journal of Remote Sensing, 16 (13), pp. 2317-2340.
[RD41]	Viallefont-Robinet, F. 2003. Removal of aliasing effect on MTF measurement using bi-resolution images. In SPIE Conference "Sensors, Systems, and Next-Generation Satellites VII", February, pp. 468-479.
[RD42]	Wald L., Monget J.M., 1983, *Sea surface winds from sun glitter observations*. Journal of Geophysical Research, 88, C4, pp. 2547-2555.
[RD43]	Wald L., 1989. *Some examples of the use of structure functions in the analysis of satellite images of the ocean*. Photogrammetric Engineering and Remote Sensing, 55, pp. 1487-1490.

[RD44]	Wald L., 1998. In-flight interband calibration of the AVHRR data by a cloud-viewing technique. *In Proceedings, EARSeL Symposium 1997 " Future Trends in Remote Sensing "*, Lyngby, Denmark, P. Gudmansen Ed., A. A. Balkema Publ., pp. 453-459.
[RD45]	Wald L., 1999. *Some terms of reference in data fusion*. IEEE Transactions on Geosciences and Remote Sensing, 37, 3, pp. 1190-1193.

Table 1:   Table of the Reference Documents.

2. MODULATION TRANSFER FUNCTION (MTF) ESTIMATION

2.1 Definition and relationships between MTF, PSF, LSF and ESF

The aim of this sub-section is to give some definitions about MTF, PSF and their relationships with the Line Spread Function (LSF) and the Edge Spread Function (ESF).

By definition, the MTF is the modulus of the Fourier Transform of the Point Spread Function:

$$
\begin{aligned}
\mathrm{MTF}\left(f_x, f_y\right) &= \left| \mathrm{FT}\left[\mathrm{PSF}\right]\left(f_x, f_y\right) \right| \\
&= \left| \iint \mathrm{PSF}(x, y)\, e^{-2i\pi\left(f_x x + f_y y\right)} dx dy \right|
\end{aligned}
$$

(Eq. 1)

The PSF corresponds to the impulse response of the optical imagery system that behaves, at least at a first order of approximation, like a low-pass linear filter; this linear filter is entirely described by its impulse response.

The PSF includes different blur effects, such as optical (diffraction and aberrations), detector spatial and temporal integration and motion blur effects.

In general case, the PSF is not symmetrical: its Fourier Transform, which corresponds to the Transfer Function of the imagery system, is therefore complex and not real. Its modulus, the MTF, is thus only partial information of the PSF that only focuses on Fourier spectral contrast.

The Line Spread Function is defined for an given orientation θ and corresponds to the integration of the PSF over the orthogonal to the direction θ (see figure 1):

$$
\begin{aligned}
\mathrm{LSF}[\theta](u) &= \int \mathrm{PSF}[\theta](u, v)\, dv \\
&= \int \mathrm{PSF}(\cos\theta\, u - \sin\theta\, v, \sin\theta\, u + \cos\theta\, v)\, dv
\end{aligned}
$$

(Eq. 2)

Two particular cases of LSF are the horizontal and vertical direction LSF:

$$
\begin{aligned}
\mathrm{LSF}[0](u) &= \int \mathrm{PSF}(u, v)\, dv \\
\mathrm{LSF}[\pi/2](u) &= \int \mathrm{PSF}(v, u)\, dv
\end{aligned}
$$

(Eq. 3)

These two particular directions are important because it corresponds to the two separable axes of the detector and the motion blur MTF.
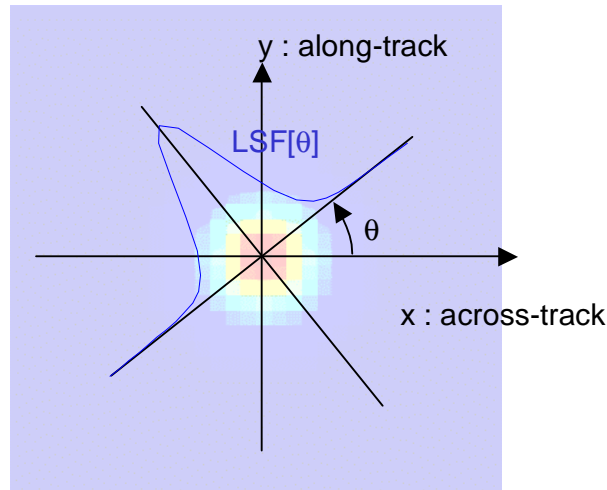
Figure 1:   LSF defined as the directional 1D PSF.

The modulus of the Fourier Transform of the $\text{LSF}[\theta]$ corresponds to a cross-section of the MTF in the direction θ :

$$\begin{aligned}
\text{MTF}[\theta](f) &= \text{MTF}(f\cos\theta, f\sin\theta) \\
&= \left| \text{FT}\big[\text{LSF}[\theta]\big](f) \right|
\end{aligned}$$

(Eq. 4)

2.2   Review of MTF estimation methods

2.2.1   General mathematical framework for MTF estimation

In the first part of this sub-section, a general mathematical framework based on Wiener filter is given. This approach is interesting because, in addition of the MTF estimation, it gives estimation the error of the MTF absolute estimation, without taking into account MTF / PSF / LSF or ESF models: those models are meant to avoid or, at least, reduce, the impact of measurement noise and aliasing effects on the MTF absolute estimation.

Without loss of generality, the above expressions are expressed in one dimension with an imagery system of sampling frequency normalized to one (GSD = 1).

Let consider the vector m_η of size N_η as the image of the target o acquired by an imagery system with a PSF noted h and measurement noise n with an over-sampling factor with respect to the native sampling frequency. This over-sampling factor is noted η.

$$\begin{aligned}
m_\eta(k) &= \int h(x)o\left(\frac{k}{\eta} - x\right)dx + n(k) \qquad\qquad k \in [0, N_\eta - 1] \\
&= h * o\left(\frac{k}{\eta}\right) + n(k)
\end{aligned}$$

(Eq. 5)

The noise n is assumed to be an independent white Gaussian noise of standard deviation σ_n.

The Transfer Function of the imagery system, defined as the Fourier Transform of its PSF h is noted H. Its modulus |H| corresponds to the MTF.

It will be assumed hereinafter that all stochastic processes inducing stochastic variability of the PSF and of the noise are stationary and real.

In the framework of the Wiener filter (*cf.* [RD30]), we wish to estimate the PSF h – or, in a dual manner, the MTF |H| – with the best mean-square error linear combination of data from the image m, *knowing* the target o.

In other words, the PSF (or LSF) estimation from an image of the known target can be seen as a deconvolution problem. The optimal deconvolution kernel in term of the mean square error is given by the Wiener filter.

The optimal Wiener Filter is defined in the Fourier interval $\left[-\dfrac{\eta}{2}, \dfrac{\eta}{2}\right]$ by:

$$G_\eta(f) = \frac{S_H(f)\widehat{O}(f)^*}{S_H(f)\left|\widehat{O}(f)\right|^2 + \sigma_n^2 + \underbrace{\sum_{k\in\mathbb{Z}} S_H(f-k\eta)\left|\widehat{O}(f-k\eta)\right|^2}_{S_A(f)}} \qquad \text{(Eq. 6)}$$

where:

- $S_H(f) = E\left[\left|H(f)\right|^2\right]$ is the expected value of the square MTF;

- $\widehat{O}$ is the Fourier Transform of the target o;

- $S_A(f)$ is the Power Spectral Density the aliasing effects, if any, taking into account possible over-sampling factor η.

The Power Spectral Density the aliasing effects is defined by the Poisson's formula:

$$S_A(f) = \sum_{k\in\mathbb{Z}^*} S_H(f-\eta k)\widehat{O}(f-\eta k) \qquad \text{(Eq. 7)}$$

From this previous expression, one can demonstrate that the mean square error of the MTF estimation is given by:

$$MSE_{MTF}(f) = N_\eta \frac{S_H(f)\left(\sigma_n^2 + S_A(f)\right)}{S_H(f)\left|\widehat{O}(f)\right|^2 + \sigma_n^2 + S_A(f)} \qquad \text{(Eq. 8)}$$

There is no aliasing effect if the over-sampling is high enough to respect the sufficient condition of the Shannon theorem.

Considering the cut-off frequency – inherent for optical imagery systems – in the spatial frequency domain of the focal plane:

$$F_c = \frac{1}{\lambda_{min}N} \qquad \text{(Eq. 9)}$$

Where:

- λ_{min} is the shortest wavelength for the considered spectral channel;

- N is the F-Number of the optical system defined as the ratio of the aperture's diameter with the focal length.

The Shannon sampling condition (*cf.* [RD30]) implies that:

$$\frac{\eta}{\delta} \geq 2F_c \qquad \text{(Eq. 10)}$$

Therefore, the oversampling factor should verify:

$$\eta \geq 2\delta \frac{1}{\lambda_{min} N} = 2\delta \frac{D}{\lambda_{min} F} = 2GSD \frac{D}{\lambda_{min} H_{sat}} \qquad \text{(Eq. 11)}$$

Under this Shannon's condition of over-sampling, the optimal mean square error of the MTF estimation is therefore:

$$MSE_{MTF}(f) = N_\eta \frac{S_H(f)\sigma_n^2}{S_H(f)\left|\widehat{O}(f)\right|^2 + \sigma_n^2} \qquad \text{(Eq. 12)}$$

The relative root mean square error, noted rMSE$_{MTF}$, is then defined by:

$$rRMSE_{MTF}(f) = \sqrt{N_\eta}\,\sigma_n \left(S_H(f)\left|\widehat{O}(f)\right|^2 + \sigma_n^2\right)^{-1/2} \qquad \text{(Eq. 13)}$$

Those expressions of the mean square error (Eq. 8) and (Eq. 12), respectively with or without aliasing effects are important because it gives very general information of the "raw" direct – *i.e.* without *a priori* model – MTF estimation, before the use of optimization with MTF models.

In particular, the estimation of the mean square error of the MTF estimator could be useful to determine the frequency range where MTF model should be optimized.

2.2.2 Target based absolute MTF estimation methods

Most of the absolute MTF in-orbit measurement methods are based on image analysis from acquisition(s) of specific well known targets. Those targets can be either:

- dedicated targets such as "on-purpose" painted surfaces, tarps, single or multiple spotlights, convex mirror array, etc.;

- artificial objects such as bridges, buildings, runway painted lines, etc.;

- or even natural objects such as fields, stars, etc.

Let consider now the two main targets used for MTF estimation:

- The pulse target;

- The edge target.

Other targets such as impulse targets, three-bar patterns or Siemens star patterns presented in the WP210 can be "simply" derived from the pulse target.

Without loss of generality, the GSD of the imagery system will be considered to be equal to one. In other words, the different dimensions related to the MTF targets will be in fact expressed as multiples of GSD.

2.2.3 The pulse target

As already presented in the WP210, and illustrated by the figure 2, a pulse target consists of a bright region surrounded by dark regions.

The main key parameters of the pulse target are:

- the differential radiance ΔL between the dark and bright parts of the target;

- the width of the pulse, noted W;

- the orientation angle α with respect to the direction of the MTF profile;

- the height L_H of the target in the orthogonal direction of the MTF profile.

Figure 2:   Pulse target for MTF estimation.

The image m of this target is therefore a set of L_H sampled LSFs in the direction of the MTF profile convoluted by the pulse of width W. Those convoluted LSFs are noted hereinafter $LSF * \pi_W$: each line m_n of the image of the pulse target can be written as:

$$m_n(k) = LSF * \pi_W\left(k + x_0 + n / \tan(\alpha)\right) + n(k)$$ (Eq. 14)

The orientation angle α conditions the maximum over-sampling factor of the $LSF * \pi_W$ along the direction of the MTF profile (*cf.* figure 3) :

$$\eta \leq \eta_{max}(\alpha) = \tan(\alpha)$$ (Eq. 15)
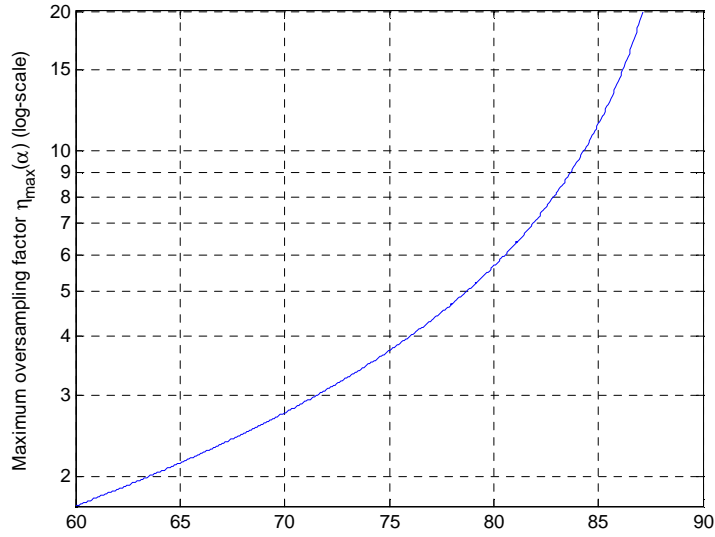
Figure 3: **Maximum over-sampling factor depending on the orientation angle with respect to the MTF profile.**

There is an important trade-off between the effective chosen over-sampling factor η and the noise regularisation to improve the SNR budget of the reconstructed over-sampled profile.

Indeed, choosing an over-sampling factor η less than the maximum one enables to "stack" different $\text{LSF} * \pi_W$ noisy profiles for a same sampling phase.

In the mean, each sub-sampling of the resulting reconstructed over-sampled $\text{LSF} * \pi_W$ profile is the results of the binning of $\lfloor L_H/\eta \rfloor$ real samplings from original noisy $\text{LSF} * \pi_W$ profiles[1]. In other words, this binning improves the SNR budget: the resulting standard deviation of the noise of the stacked and over-sampled $\text{LSF} * \pi_W$ profile, noted σ_η verifies:

$$\sigma_\eta = \sigma_n \Big/ \sqrt{\lfloor L_H/\eta \rfloor} \approx \sigma_n \sqrt{\frac{\eta}{L_H}} \qquad \text{(Eq. 16)}$$

A good compromise is to set the over-sampling factor to the smallest value (with an optional margin) enabled by the sampling condition of Shannon (Eq. 11), in order to maximize the noise reduction by stacking the L_H noisy profiles. Of course, this can be done provided that this "optimal" over-sampling factor is less than the maximum over-sampling factor conditioned by the orientation angle α of the target:

$$\eta_{opt} = \min\left(\tan(\alpha), \frac{2\delta}{\lambda_{min}N}(1 + \text{Margin}) \right) \qquad \text{(Eq. 17)}$$

---

[1] $\lfloor \ \rfloor$ *stands for the floor rounding operator.*

To those main key parameters, one should also consider:

- the length of the pulse target L_W (in the direction of the MTF profile): this length should be larger than the spatial extension of the PSF, defined in the WP210, as the twice the PSF extend radius. This minimum length is defined in order to prevent the LSF from being truncated. In this study, we propose to define this PSF extend radius as the 95 % energy encircled radius in pixels;

- the length L_T of the dark area surrounding the "core" target to prevent the surrounding background from "contaminating" the image of the pulse target. This length should be greater than the PSF extend radius.

Once the $LSF * \pi_W$ profile has been computed by stacking and interleaving the different sampling phases, we have at "our disposal" a 1D $LSF * \pi_W$ profile over-sampled by the factor η with a reduced Gaussian noise n_η of standard deviation σ_η:

$$m_\eta(k) = LSF * \pi_W(x_0 + k/\eta) + n_\eta(k) \qquad \text{(Eq. 18)}$$

Therefore, the estimation of the LSF from the reconstructed over-sampled $LSF * \pi_W$ profile can be made with the "signal" deconvolution approach developed in the sub-section §2.2.1. The regularization with a MTF / PSF / LSF or even ESF model can be done after the signal processing stage.

The modulus of Fourier Transform of the over-sampled "known object" π_W, noted $\widehat{\Pi}_W$ verifies, in the Fourier interval $\left[-\dfrac{\eta}{2}, \dfrac{\eta}{2}\right]$:

$$\left|\widehat{\Pi}_W(f)\right| = \Delta L \frac{\sin(\pi W f)}{\sin(\pi f/\eta)} \approx \Delta L \, W \eta \, \mathrm{sinc}(Wf) \qquad \text{(Eq. 19)}$$

Then, applying the equation (Eq. 12), the mean square error of the MTF estimator is, then:

$$MSE_{MTF}(f) = \frac{E\left[\left|H(f)\right|^2\right]}{\left(E\left[\left|H(f)\right|^2\right]\left(\dfrac{\Delta L}{\sigma_n}\right)^2 W^2 \dfrac{\eta}{L_w} \mathrm{sinc}(Wf)^2 + 1\right)} \qquad \text{(Eq. 20)}$$

One can note that, on account of the sinc, if the size in pixel W of the pulse target is close to an even number, sinc(Wf) is close to zero in the neighbourhood of the Nyquist frequency. The mean square error of the MTF estimator is then close to the expected value of the square of the MTF. It means that, in the case of pulse target's width close to even multiple of the GSD, the relative root mean square error of the MTF estimator, rRMSE$_{MTF}$(0.5) at the Nyquist frequency is equal to 100 % !

As an illustration, we have simulated the case of MTF estimation with six pulse targets of different widths (0.2, 0.5, 1, 2, 3 and 5 GSD) with two different ratios $\Delta L/\sigma_\eta$ (50 and 200).

The figure 4 gives the corresponding relative root mean square error of the MTF estimator in log-scale for different normalized spatial frequencies up to the Nyquist frequency (red: $\Delta L/\sigma_{LSF}(\eta) = 50$, blue: $\Delta L/\sigma_{LSF}(\eta) = 200$).
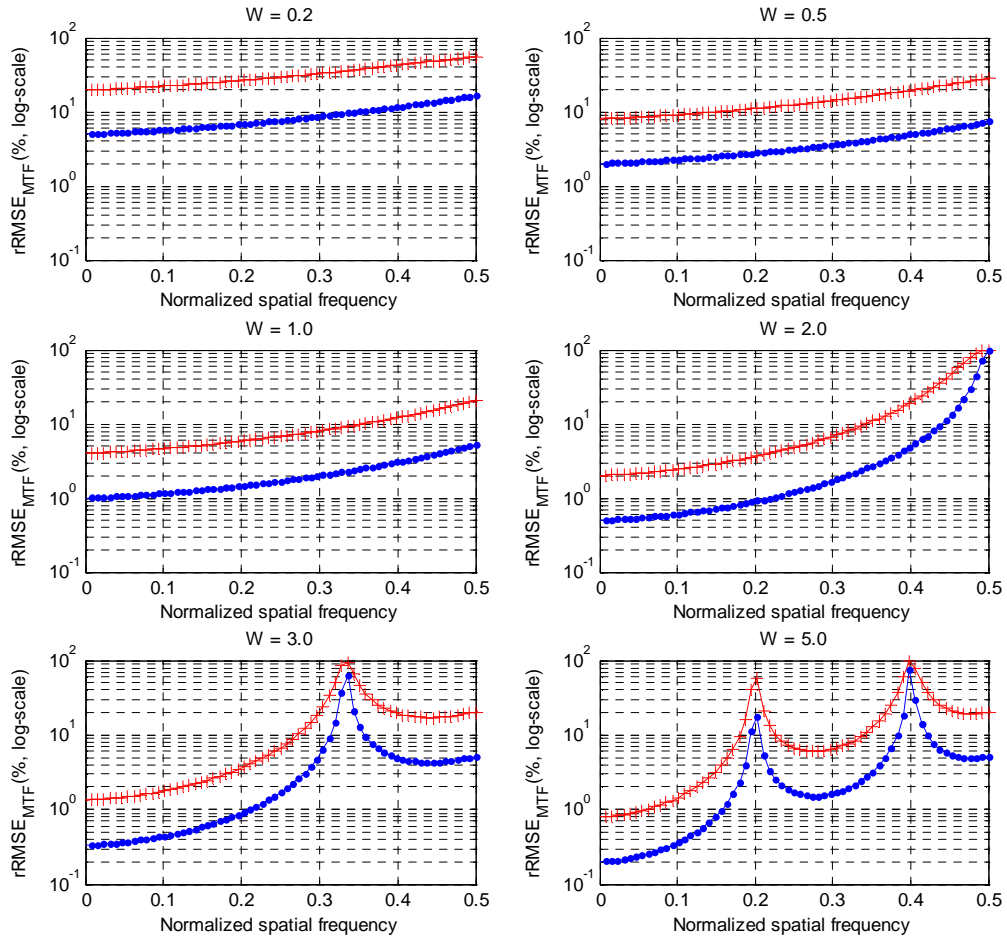
Figure 4: Relative root mean square error of the MTF estimator rRMSE$_{MTF}$ for different widths of pulse target and for two ratios $\Delta L/\sigma_{LSF}(\eta)$ (red: 50, blue: 200).

This example shows that the accuracy of the MTF estimation for a particular spatial frequency strongly depends on the width of the pulse target.

More precisely, on account of zero-crossing of the Fourier transform of the pulse, the relative root mean square error of the MTF estimator is close to 100 % for frequencies in the neighbourhood of multiples of the inverse of the pulse's width:

$$\left\{ \frac{k}{W}, k \in \mathbb{N} \right\} \tag{Eq. 21}$$

Inversely, the Fourier transform of the pulse has local maxima for odd multiple of the inverse of twice the pulse's width. The neighbourhood of those frequencies are therefore the most suitable frequencies for the MTF estimation.

$$\left\{ \frac{2k+1}{2W}, k \in \mathbb{N} \right\} \tag{Eq. 22}$$

2.2.4 The edge target
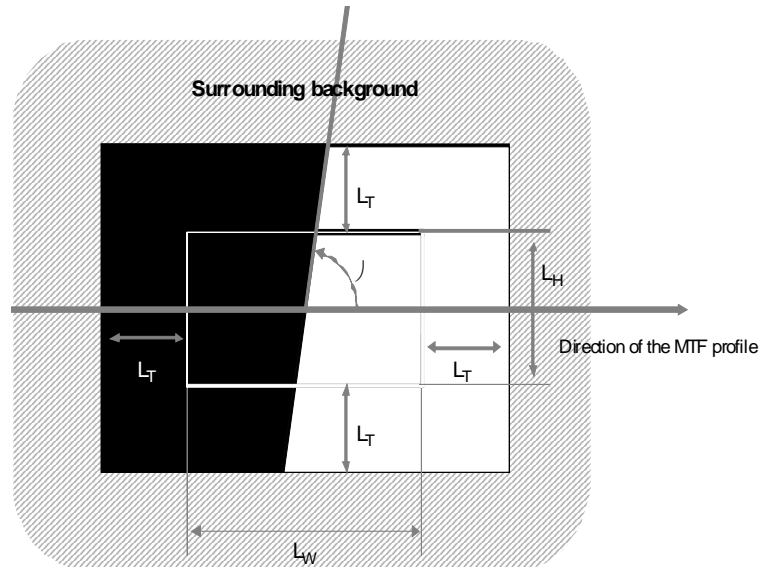
Figure 5:   Edge target for MTF estimation.

An edge target corresponds to a high contrast Heaviside edge (*cf.* figure 5). The main key parameters of the pulse target are:

- the differential radiance ΔL between the dark and bright part of the target;

- the width of the target in the direction of the MTF profile, noted L_W;

- the orientation angle α with respect to the direction of the MTF profile;

- the height L_H of the target in the orthogonal direction of the MTF profile.

The tradeoff between the orientation angle and the height of the target is exactly the same as the one for the pulse target presented in the previous sub-section 2.2.3.

The image m of an edge target is therefore a set of L_H sampled LSFs, in the direction of the MTF profile, convoluted by the Heaviside function u.

Those convoluted LSF is called hereinafter ESF for Edge Spread Function. Each line of the image of the pulse target are therefore noisy sampled ESF and can be written as:

$$m_n(k) = ESF\big(k + x_0 + n/\tan(\alpha)\big) + n(k)$$
$$= LSF * u\big(k + x_0 + n/\tan(\alpha)\big) + n(k) \qquad \text{(Eq. 23)}$$

Again, the estimation of the LSF from the reconstructed over-sampled ESF profile can be made with the "signal" deconvolution approach developed in the sub-section §2.2.1:

$$m_\eta(k) = ESF\big(x_0 + k/\eta\big) + n_\eta(k)$$
$$= LSF * u\big(x_0 + k/\eta\big) + n_\eta(k) \qquad \text{(Eq. 24)}$$

Where n_η is an independent Gaussian noise whose standard deviation is noted σ_η.

The modulus of the Fourier Transform of the Heaviside function truncated (of width L_W) and over-sampled by a factor η is:

$$\left|\hat{U}(f)\right| = \Delta L \frac{\sin\left(\pi L_W f/2\right)}{\sin\left(f/\eta\right)} \qquad \text{(Eq. 25)}$$

For spatial frequencies that are close to odd multiples of the inverse of the edge's width L_W, this modulus of the Fourier Transform can be approximated by:

$$f \approx \frac{2k+1}{L_W}, k \in \mathbb{N}, \left|\hat{U}(f)\right| \approx \frac{\Delta L \eta}{\pi f} \qquad \text{(Eq. 26)}$$

Inversely, the function $\left|\hat{U}(f)\right|$ has zero-crossings for even multiples of $1/L_W$ and:

$$f \approx \frac{2k}{L_W}, k \in \mathbb{N}, \left|\hat{U}(f)\right| \approx 0 \qquad \text{(Eq. 27)}$$

As the edge's width L_W is supposed to be large with respect to the PSF's extend, the alternation between 0 and $\Delta L \eta/f$ has a small period ($1/L_W$).

The figure 6 is an example of the Fourier transform of a 16 GSD large edge target, over-sampled by a factor 4.
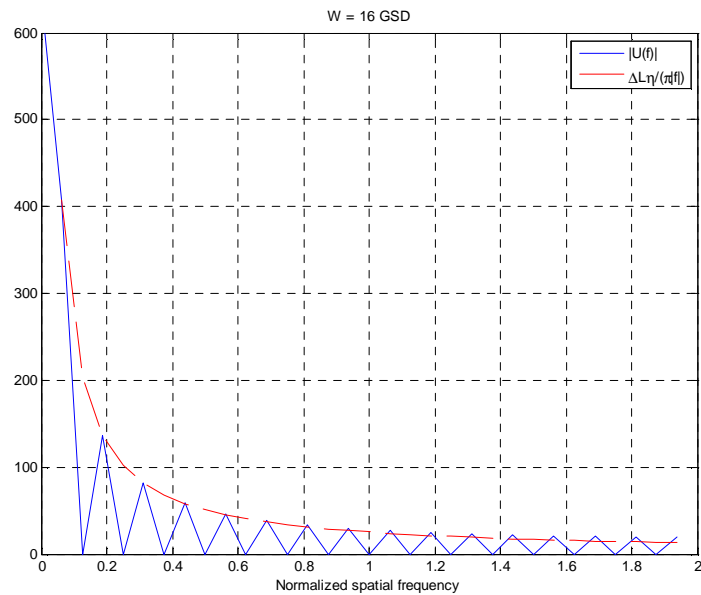

Figure 6:   **Modulus of the Fourier Transform of the sampled and truncated (LW = 16 GSD) and over-sampled (η =4) Heaviside function.**

Therefore, for suitable frequencies, *i.e.* in the neighbourhood of odd multiples of $1/L_W$, the relative root mean square error of the MTF estimation is:

$$rRMSE_{MTF}\left(f \approx \frac{2k+1}{L_W}\right) = \frac{\sigma_\eta\sqrt{L_W\eta}}{\sqrt{E\left[|H(f)|^2\left(\frac{\Delta L\eta}{\pi f}\right)^2 + L_W\eta\sigma_\eta^2\right]}}$$

(Eq. 28)

It is interesting to note that this optimal relative root mean square error of the MTF estimation is obtained by the Wiener filter derived from the equation (Eq. 6), without the aliasing term of error.

In literature (*e.g.* [RD13], [RD15], [RD14]), the standard approach to estimate the LSF from the ESF reconstructed is the convolution with the first order derivative filter $h_{\partial 1}$:

$$h_{\partial 1} = \left[-\frac{1}{2\Delta L} \quad 0 \quad \frac{1}{2\Delta L}\right]$$

$$\hat{H}_{\partial 1}(f) = \frac{i}{2\Delta L}\sin(2\pi f/\eta) \underset{f\sim 0}{\approx} i\frac{\pi f}{\Delta L\eta}$$

(Eq. 29)

As shown by the previous equation, this derivative filter approximates, for small values of spatial frequency, the inverse of the Fourier Transform of the Heaviside function.

Nevertheless, this filter does not take into account neither the zero-crossings nor the radiometric noise n_η.

The figure 7 represents an example of a Wiener filter compared to the first order derivative filter and to the "strict" inverse filter. The Wiener filter takes into account:

- the zero-crossings for even multiples of $1/L_W$: for those frequencies, the Wiener filter is null;

- the standard deviation of the noise: considering this standard deviation with respect to the radiance differential ΔL, the Wiener filter "stops" the deconvolution after the normalized spatial frequency 0.6 and completely damps the signal beyond the normalized spatial frequency 1. Of course, this is an example: the deconvolution and damping bandwidth of the Wiener filter strongly depends on the SNR of the profile.
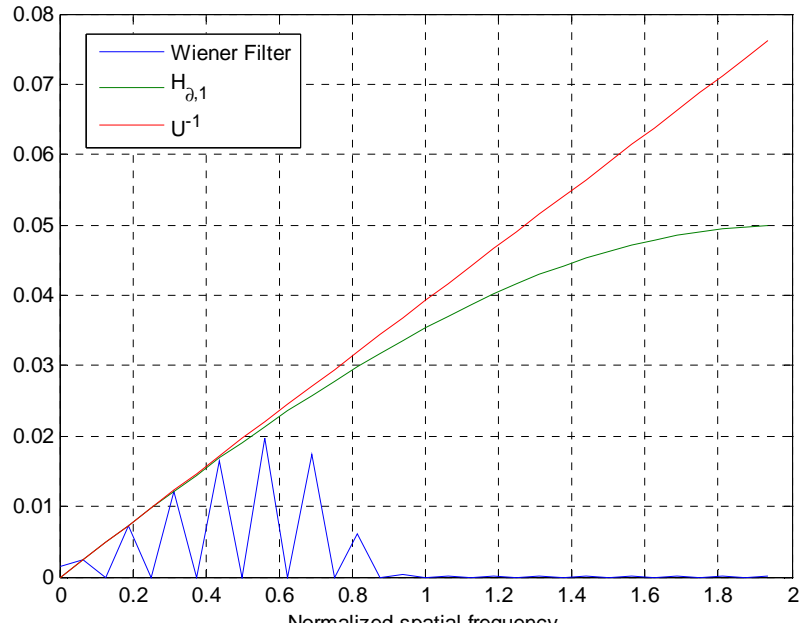
Figure 7: **Examples of transfer functions (modulus) of the first order derivative filter (green line) and the Wiener filter (blue line). Those transfer functions are compared to the inverse filter of the Heaviside function u (red line).**

The resulting relative root mean square errors for those three approaches for the deconvolution of the ESF profile are given in the figure 8. Only odd multiples of $1/L_W$ frequencies have been considered here. The Wiener approach is obviously the optimal approach and the first order derivative gives the worst results.
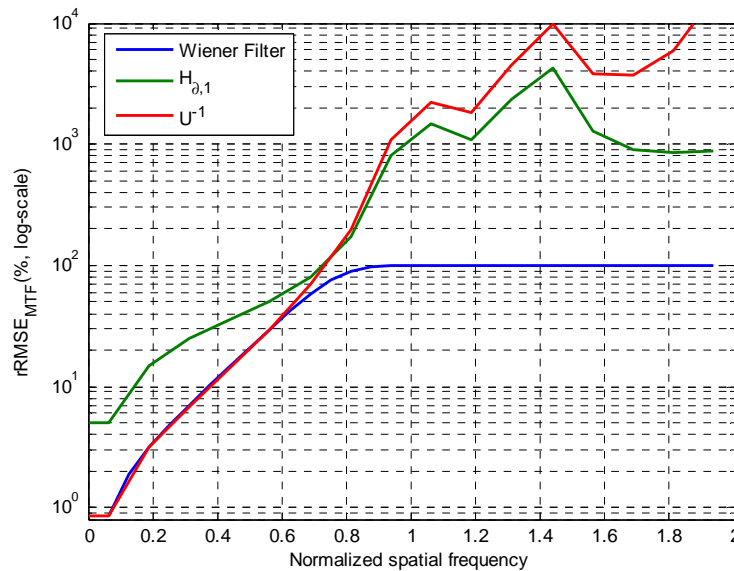
Figure 8: **Examples of relative root mean square errors (in %, in log-scale) for the three different deconvolution kernels (Wiener, first order derivative and inverse kernels) presented in the figure 7.**

For the same characteristics of the radiometric noise and target's size L_W, a performance comparison has been made between the edge target and three pulse targets of widths ½ GSD, GSD and 3 GSD (*cf.* figure 9).

The resulting performances for those four targets are presented in the figure 10. Those performances are formulated in terms of theoretical relative root mean square error of the four different MTF estimations.

(a)

(b)

(c)

(d)
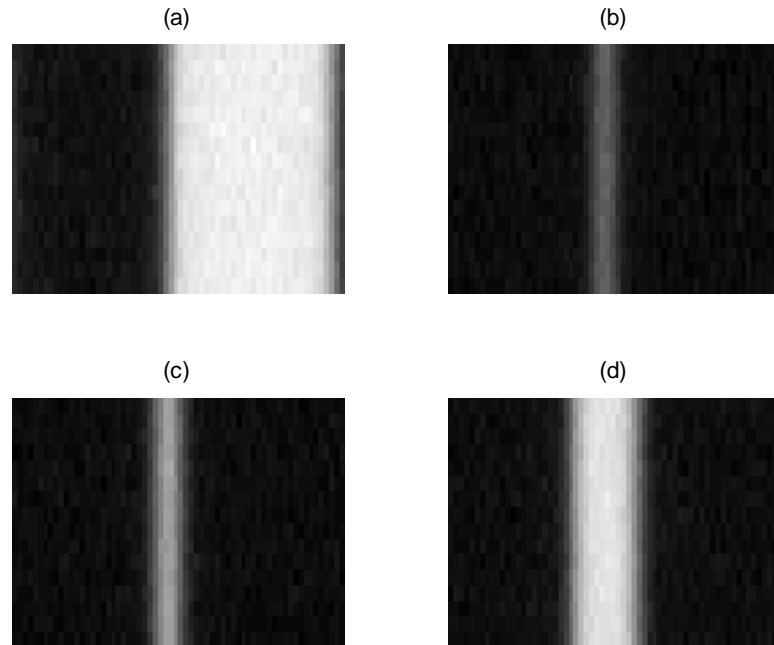
Figure 9: **(a) Edge target. (b) Pulse target (W = 1/2 GSD). (c) Pulse target (W = GSD). (d) Pulse target (W = 3 GSD).**
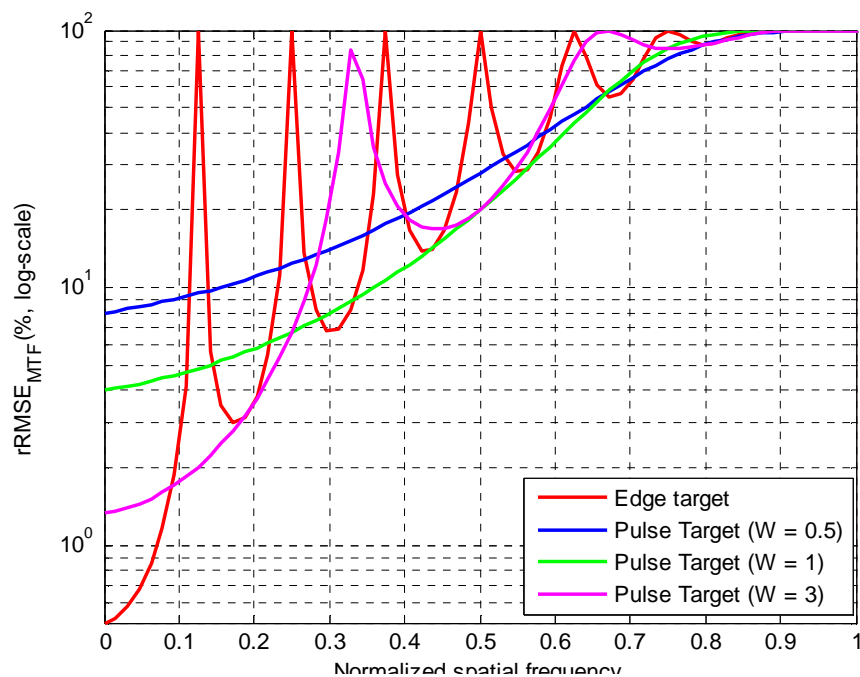
Figure 10: Resulting relative root mean square error rRMSE$_{MTF}$(f) for the four targets presented in the figure 9.

2.2.5 Bi-resolution MTF estimation methods

The bi-resolution MTF estimation method makes use of spectrum ratios in the Fourier domain of two images of the same scene in order to estimate the ratio of their respective MTF. Of course, this approach requires specific pre-processing such as geometric registration and radiometric alignment. Change detection algorithm could be also used to determine areas that are temporally stable between the two image acquisitions.

This approach can be used for two different cases. In the first case, the two MTF of the two images are unknown and their respective GSD are comparable. In this case, of course, only relative MTF estimation can be done. As noticed by Léger et al. [RD23], this method has been used for SPOT systems to estimate temporal evolution of the MTF due to, for example, defocus degradation or spatial MTF variation in the field of view of the instrument.

In the second case, one of the two images has a higher resolution, typically, at least a factor 5 between the GSDs. In this case, even if the MTF of the high resolution (HR) image is unknown, it is assumed to be equal to one, at the scale of the low resolution image (LR). In other words, this approach enables an absolute MTF estimation of the LR image.

This method has been used for the SPOT 4 commissioning phase presented by Kubik *et al.* [RD18] to assess the VEGETATION's MTF with the HRG image.

To apply this method, a direct approach consists in first estimating the Power Spectrum Density (PSD) of the two co-registred images. Those PSD estimations can be achieved by the Welch method (cf. [RD30]). The square root of the ratio of the two PSD is then an estimation of the ratio of the two MTFs.

As noticed by Kubik *et al.* [RD18] and confirmed by Léger et al. [RD23], this "direct" application of the bi-resolution method suffered from an over-estimation of the MTF due to aliasing effects.

To compensate for this aliasing effects inducing over-estimation of the MTF near the Nyquist frequency, Viallefont-Robinet, in [RD41], proposed a bi-resolution method taking into account PSD estimation of the aliasing component in LR image for the MTF estimation, in order to avoid its over-estimation.

2.2.6 "Blind" absolute MTF estimation methods with specific on-board devices

There exist some specific devices meant to estimate the MTF without having requirement about the knowledge of the observed scene or object: in this case, those approaches are called "blind" method.

An example of those "blind" approaches requiring specific on-board devices is the phase diversity method. Precisely described by Paxman *et al.* [RD31], this image processing technique infers the global MTF from a set of more than two concomitant image acquisitions of the same extended object or "rich" natural scenes (*e.g.* urban areas).

The first matrix image acquisition corresponds to a "standard" focal-plane acquisition. Therefore, this acquisition takes into account the unknown MTF / PSF.

The other acquisitions are made with additional known perturbations of the MTF. A simple way to do this is to translate the other detector matrixes in the focal plane to induce different known defocuses for the secondary image acquisitions.

Practically, the image processing corresponds to a joint and iterative estimation of:

- the unknown scene, via a deconvolution processing taking into account of the previous MTF estimation ;

- the MTF, *via* a Zernike model as described in the sub-section §2.3.1 (Eq. 36) and (Eq. 37), taking into account the current estimation of the unknown object.

Those two conjoint estimations are iterated until convergence.

2.3 Direct and indirect parametric models of the MTF

Different models of MTF exist in the bibliography. Those models can be direct 2D MTF models, or indirectly, through LSF or ESF parametric 1D models. The aim of this sub-section is to synthesize those different parametric models.

Those parametric models can be fitted on the "raw" MTF / PSF / LSF or ESF estimated by the signal processing approach. There exists many optimization approaches to determine those parametric models. The most widely used methods are:

- *The downhill simplex method*: this multidimensional optimization method does not use the gradient of the cost function that have to be optimized: it is therefore useful for non smooth (noisy) or discontinuous cost functions;

- *Levenberg-Marquardt method*: this multidimensional optimization method is a gradient and hessian based method. The gradient and the hessian of the cost-function should be given or numerically estimated.

See [RD33] for details for both optimization algorithms.

2.3.1 Parametric 2D MTF models

Blanc and Delvit *et al.* in [RD7] and [RD8] have proposed a simplified 2-parameter 2D MTF models:

$$\mathrm{MTF}\left(f_x, f_y\right) = \underbrace{\exp\left(-\sqrt{\left(\lambda_x f_x\right)^2 + \left(\lambda_x f_x\right)^2}\right)}_{A}\underbrace{\mathrm{sinc}\left(f_x\right)}_{B}\underbrace{\mathrm{sinc}\left(f_y\right)^2}_{C} \qquad \text{(Eq. 30)}$$

where:

- $\mathrm{sinc}\left(x\right) \overset{\Delta}{=} \sin\left(\pi x\right)/\left(\pi x\right)$

- f_x and f_y are spatial frequencies normalized by the sampling frequency, respectively across-track and along-track.

The expression A stands for an approximation of the *optical MTF* including the diffraction phenomena and different optical errors sources such as aberrations, decentring or focusing.

The expression B is an approximation of the detector MTF defined as the MTF degradation due to the spatial integrator effect across-track of the detector.

The expression C is an approximation of the detector MTF along-track – $\mathrm{sinc}(f_y)$ – combined with the smearing along-track effects due to detector displacement during the integration time.

Léger *et al.* [RD22] proposes a complementary model in order to take into account more precisely a possible defocus Δ_{focus} of the optical system:

$$\mathrm{MTF}_{\mathrm{defoc}}\left(\rho\left(f_x, f_y\right)\right) = 2J_{1c}\left(X\left(\rho\left(f_x, f_y\right)\right)\right) \qquad \text{(Eq. 31)}$$

where:

- $\rho\left(f_x, f_y\right) = \sqrt{f_x^{\,2} + f_y^{\,2}}$

- $J_{1c}\left(x\right) = J_1\left(\pi x\right)/\left(\pi x\right)$ and $J_1\left(x\right) = \dfrac{1}{\pi}\displaystyle\int_0^{\pi}\cos\left(\tau - x\sin\tau\right)\mathrm{d}\tau$ is the first order J-Bessel function;

- $X\left(\Delta, f\right) = \dfrac{\Delta}{N\delta}f\left(1 - \dfrac{\lambda N}{\delta}f\right)$;

- λ is the central wavelength;

- δ is the detector size (in the focal plane);

- N is the F-number.

As far as the detector MTF is concerned, a more accurate standard model is a 1 parameter trapezoid detector model:

$$\mathrm{MTF}_{det}\left(f\right) = \mathrm{sinc}\left(f\right)\mathrm{sinc}\left(\alpha_{det}f\right) \qquad\qquad (Eq.\ 32)$$

To take into account a possible multi-phase Time Delay Integration sub-system (*e.g.* PLEIADES system) or an integration time less than the line sampling time, the smearing along-track MTF model can be a 1 parameter model:

$$\mathrm{MTF}_{sm}\left(f_y\right) = \mathrm{sinc}\left(\alpha_{sm}f_y\right) \qquad\qquad (Eq.\ 33)$$

Moreover, especially for High Resolution System (metric and sub-metric) with a "large" Time Delay Integration sub-system, an additional MTF degradation has to be considered.

This specific MTF degradation is related to the motion blur due to line of sight temporal perturbations during the integration time. Precise model of motion blur, sometimes called desynchronization MTF for High Resolution TDI imagery system such as PLEIADES-HR, can be very complex, depending on the high or low frequency nature of the perturbations with respect to the integration time (*cf.* [RD37]).

The equation below corresponds to a simple model, based upon a low frequency perturbation assumption:

$$\mathrm{MTF}_{mb}\left(f\right) = \mathrm{sinc}\left(\alpha_{mb}f\right) \qquad\qquad (Eq.\ 34)$$

The combination of those models, leading to a 7-parameter model, can improve the accuracy and the relevancy of the MTF model:

$$
\begin{aligned}
\mathrm{MTF}(f) = {}& \exp\left(-\sqrt{\left(\lambda_x f_x\right)^2 + \left(\lambda_x f_x\right)^2}\right)\mathrm{MTF}_{defoc}\left(\rho\left(f_x, f_y\right)\right) && \left[\mathrm{MTF}_{opt}\right]\\
& \mathrm{sinc}\left(f_x\right)\mathrm{sinc}\left(\alpha_{det}f_x\right) && \left[\mathrm{MTF}_{det}\right]\\
& \mathrm{sinc}\left(f_y\right)\mathrm{sinc}\left(\alpha_{det}f_y\right) && \left[\mathrm{MTF}_{det}\right] \qquad (Eq.\ 35)\\
& \mathrm{sinc}\left(\alpha_{sm}f_y\right) && \left[\mathrm{MTF}_{sm}\right]\\
& \mathrm{sinc}\left(\alpha_{mbx}f_x\right)\mathrm{sinc}\left(\alpha_{mby}f_y\right) && \left[\mathrm{MTF}_{mb}\right]
\end{aligned}
$$

It is important to note that the instrument is partially known thanks to the detailed optical design and the on-ground calibration of sub-systems such as detectors unit and are not prone to change in-orbit.

In other words, some of those parameters has not to be estimated during the in-orbit MTF assessment. Usually, the detector and the smearing along-track MTF degradation are stable and well known. Therefore, their corresponding model parameters have not to be estimated during the in-orbit optimization of the MTF model.

The previous optical MTF model, even with its improvement based on a defocus MTF model, is very simple. Mugnier and Le Besnerais [RD27] have proposed, for the optical MTF, a « physical » multi-parameter model based on a Zernike orthonormal decomposition of the wave-front error (WFE) that corresponds to the optical aberration in the entrance annular pupil of the instrument:

$$\mathrm{WFE}\left(p\right) = \sum_{l=1}^{N} \gamma_l Z_{l_0+l}\left(p\right) \qquad\qquad (Eq.\ 36)$$

where:

- p corresponds to the spatial location in the pupil entrance.

In [RD27], Mugnier and Le Besnerais have limited the Zernike decomposition to 8 parameters from Z_4 (defocus) to Z_{11} (spherical decomposition).

The optical PSF is then numerically computed as the squared modulus of the Fourier transform of the complex pupil:

$$PSF_{opt}(x,y) = \left| FT\left[P(p_x,p_y) e^{-\frac{2i\pi}{\lambda}WFE(p_x,p_y)} \right]\left(-\frac{x}{\lambda F}, -\frac{y}{\lambda F} \right) \right|^2 \qquad \text{(Eq. 37)}$$

where:

- x, y corresponds to the spatial location in the focal plane;

- P is the pupil support generally circular or even annular, in the case of central obscuration of the telescope;

- λ is the central wavelength;

- δ is the detector size (in the focal plane);

- F is the focal of the instrument.

An intermediate and simpler mean to "physically" model the optical MTF is to combine a perfect diffraction limited optical MTF with a Gaussian global model of optical aberration MTF:

$$MTF_{diff-opt}(f_x,f_y) = \iint P(p_x,p_y) P\left(p_x - \frac{\lambda}{\delta F}f_x, p_y - \frac{\lambda}{\delta F}f_y \right) dp_x dp_y$$

$$MTF_{aber-opt}(f_x,f_y) = e^{-\kappa^2\left(\frac{\lambda f}{\delta F}\right)^2} \qquad \text{(Eq. 38)}$$

The figure 11 represents cross-sections of the (isotropic) diffraction limited optical MTF with different ratio ε of the central obstruction with respect to the pupil diameter.
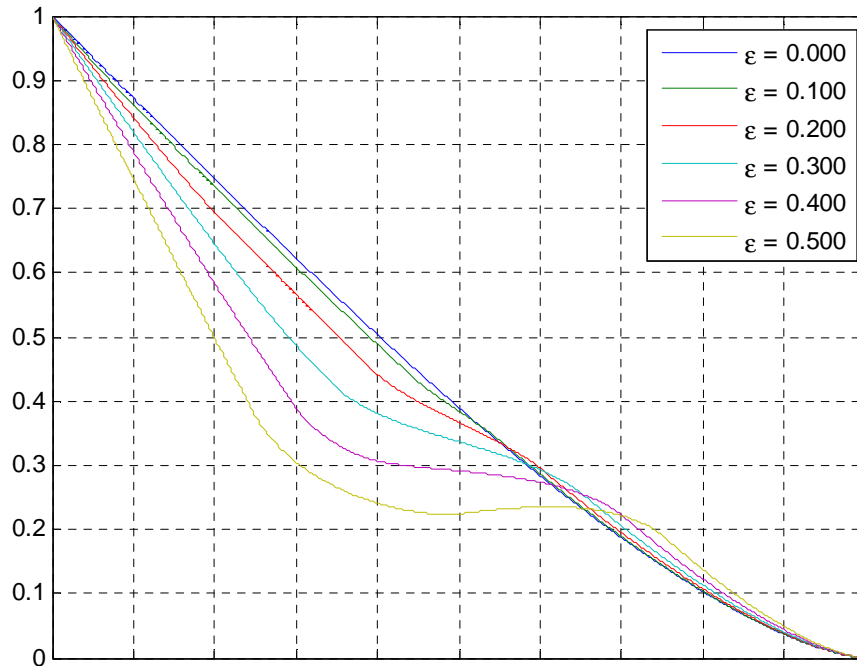
Figure 11: **Cross-section of the diffraction limited optical MTF for different ratios ε of central obscuration. Frequencies are normalized by the cut-off frequency 1/(Nλ).**

The two physical previous models have the advantage to be easily "transposed" from a spectral band to another one, by taking into account their respective central wavelengths.

Spectral sensitivity $S(\lambda)$ could be used in those physical models, instead of the central wavelength λ:

$$MTF_{diff-opt}^{S}\left(f_x, f_y\right) = \frac{\iiint S(\lambda) P\left(p_x, p_y\right) P\left(p_x - \frac{\lambda}{\delta F} f_x, p_y - \frac{\lambda}{\delta F} f_y\right) dp_x dp_y d\lambda}{\int S(\lambda) d\lambda}$$

$$MTF_{aber-opt}\left(f_x, f_y\right) = \frac{\int S(\lambda) e^{-\kappa^2 \left(\frac{\lambda f}{\delta F}\right)^2} d\lambda}{\int S(\lambda) d\lambda}$$

(Eq. 39)

2.3.2 Parametric 1D LSF or ESF models

To avoid noise and aliasing "contamination" on the MTF cross-section estimation from a edge target, different models of ESF are used in the bibliography.

Thomas [RD38] proposes a sigmoid 3-parameter model:

$$ESF(x) = \frac{1}{a_0 a_1^{x} + a_2}$$

(Eq. 40)

Leloglu and Tunali [RD24] have proposed first a "simple" 3-parameter model based on the error function erf.

$$\text{ESF}(x) = a_0 + a_1 \text{erf}(a_2 x) \qquad\qquad\qquad (\text{Eq. 41})$$

This model, also mentioned by Helder *et al.* [RD14], corresponds in fact to a gaussian model for the PSF, and, therefore, for the MTF.

This model is judged in both papers too "simple" to be able to follow high frequency effects of the ESF, like ringing or ripples near. This can be explained by the fact that the PSF with its potential skewness and secondary lobes is definitively not gaussian.

To circumvent this limitation, Leloglu and Tunali [RD24] have proposed a 6-parameter model as a combination with the erf based previous model and a fifth order odd polynomial apodized with a hamming window w:

$$\text{ESF}(x) = a_0 + a_1 \text{erf}(a_2 x) + w(x) \sum_{k=1}^{3} c_i x^{2k-1} \qquad\qquad (\text{Eq. 42})$$

Helder *et al.* [RD14] have mentioned an other 10-parameter ESF model based upon Fermi functions, of the form:

$$\text{ESF}(x) = d + \sum_{k=1}^{3} a_k \left(\exp\left(\frac{x - b_k}{c_k}\right) + 1 \right)^{-1} \qquad\qquad (\text{Eq. 43})$$

In addition to their "intrinsic" model parameters, the different ESF models should have two additional parameters: the phase shift of the ESF with respect to the sampling grid for the ESF measured in the edge target image.

3.   SIGNAL TO NOISE RATIO (SNR)

3.1   Definition of the SNR

The signal to noise ratio (SNR) is one of the elements of the image quality. It characterizes the radiometric noise. The image noise quantifies the variation of the radiances at a given radiance level for a uniform landscape. It is defined as:

$$SNR = m / \sigma \tag{Eq. 44}$$

where m is the mean of a series of radiances for this uniform landscape and σ is the standard deviation of this series.

If the imaging system is such that a line of the image is acquired by a CCD array, then the noise in the image is a combination of two separate noises (Kubik *et al.* 1998 [RD18]; Porez, Sylvander 2007 [RD32]):

- column-wise noise, also called instrumental noise: caused by Poisson fluctuation of the signal delivered by the detector and various constant electronic onboard chain noises,

- and line-wise noise, also called normalization noise; following image normalization, the residuals may cause visible 'columns' on a uniform landscape.

In this case, each noise must be assessed separately. They are then "quadratically" summed to yield a single value.

If the imaging CCD array is a matrix (*e.g.*, the PolDER system), then each CCD has its own noise. As there are several normalization steps to equalize the CCDs signal, the noise is assumed in the same way than for the line-wise noise.

The SNR is a function of the mean radiance of the landscape. The SNR is usually lower for low values of radiance (dark landscape) because the relative influence of the noise is larger. For large radiances, the SNR increases as the relative influence of the noise decreases. Accordingly, the SNR should be known at different radiance levels.

In some cases, a model can be established that relates the noise to the absolute calibration coefficient, onboard image amplification gain, and radiance. In this way, once the SNR is known for a reference radiance and neutral gain whose value is 1, it can be assessed for any radiance and gain. In the case of a CCD array, the model applies to the column-wise noise (Lebègue *et al.* 2003 [RD20]).

If there is an on-board calibration device, *e.g.*, a calibration lamp, the SNR is estimated by collecting a series of observations of this lamp. This can be done during the planned calibration sequences. The emission of the lamp is assumed to be constant during the period of collection. From this series, the mean and standard-deviation are computed and the SNR is assessed. In case of CCD arrays, this technique can only apply to column-wise noise, i.e., the time-series must be collected by the same CCD (Kubik *et al.* 1998 [RD18]). For line-wise noise, vicarious techniques should be adopted.

3.1.1   Absolute calibration for SNR estimation

The SNR is a ratio and its value depends whether it is expressed in radiances or digital counts. The SNR depends upon the quality of the absolute calibration of the instrument and in the case of CCDs array(s) of the inter-CCD and inter-array calibration. The conversion of a digital count *DC* into radiance *L* is in the form:

$$L = \alpha\ DC + \beta \qquad \text{(Eq. 45)}$$

where α is a gain and β an offset. Because β is not zero, the SNR is not equal in digital counts or in radiances. The SNR should be expressed in radiances and it cannot be generally computed with digital counts. The smaller β, the smaller the difference between the two SNRs.

3.1.2 Effects of the atmospheric extinction of radiance on SNR estimation

The radiance measured at system level depends on the optical properties of the atmosphere in both downwards and upwards directions. At first order, and under clear skies, one may write

$$L_{sat} = \tau\ L_{ground} + L_{atm} \qquad \text{(Eq. 46)}$$

where L_{sat} is the observed radiance, L_{ground} is the radiance coming from the ground, τ is the transmittance of the atmosphere and L_{atm} is the radiance due to scattering by the atmospheric constituents.

It is usually assumed that the terms τ and L_{atm} exhibit no high frequencies. Accordingly, the standard-deviation of L_{sat} is equal to

$$\sigma[L_{sat}] = \tau\ \sigma[L_{ground}] \qquad \text{(Eq. 47)}$$

Hereinafter, the operators $\sigma[\ ]$ and $m[\ ]$ denotes respectively the standard deviation and the mean of the operand.

From these equations, one conclude that

- the SNR differs whether it is computed in radiances with or without atmospheric correction. The lower L_{atm}, the smaller the difference.

- the assessment of SNR should take into account the optical effects of the constituents in the atmosphere.

The following is a rough calculation of the error δ that is committed on the SNR if computed without correction. Let denote SNR_{sat} the SNR assessed from the satellite radiances without correction. Let SNR_{actual} be the actual SNR. Assuming (Eq. 47), one obtains a relationship between, the SNR assessed from the satellite and the actual SNR:

$$
\begin{aligned}
SNR_{sat} = \frac{m}{\sigma} &= \frac{m\left[\tau L_{ground} + L_{sat}\right]}{\sigma\left[\tau L_{ground} + L_{sat}\right]} \\
&\approx \frac{m\left[\tau L_{ground} + L_{sat}\right]}{\tau\sigma\left[L_{ground}\right]} \\
&= SNR_{actual} + \delta
\end{aligned}
\qquad \text{(Eq. 48)}
$$

where δ is equal to

$$\delta = \frac{m\left[L_{atm}\right]}{\tau\sigma\left[L_{ground}\right]} \qquad \text{(Eq. 49)}$$

Assume a typical value of 150 for SNR_{actual} and a value of 0.7 for τ. Assume that L_{atm} is about 0.05 times m. Then, typically

$$\delta \approx 11 \tag{Eq. 50}$$

This rough calculation indicates the level of uncertainty that can be expected if one does not correct for atmospheric effect.

This uncertainty may also be considered close to that would be observed if the atmospheric terms L_{atm} and τ contain high frequencies. In [RD29], Panchev (1971) suggested to use the structure function to assess the intensity of the small-scale structures.

Practically, it could be applied on images acquired over sites suitable for Rayleigh calibration. During this operation, spatial homogeneity is assumed. Computing the structure function will permit to assess the heterogeneity of these atmospheric terms, though the contributions of the ocean surface may play a role.

3.2   Earth-viewing approach for SNR assessment

Only a very limited number of imaging systems has an on-board calibration device fully appropriate to the assessment of the SNR. Most often, vicarious techniques should be employed. These techniques are based on the earth-viewing approach. In this approach, an image acquired by the system, or combination of images, is used to compute the SNR. The radiance emitted by this landscape has certain properties, *e.g.*, spatial homogeneity, whose knowledge permits to assess the SNR.

Before discussing the methods to assess the SNR in the earth-viewing approach, we should study the role played by the image quality in the assessment of the SNR. As Earth-viewing techniques deal with images, there is a link between SNR, MTF and PSF. The following section shows that a minimum surface exists for an accurate assessment of the SNR.

3.3   Relationships between SNR, MTF and PSF – Minimum surface

Image quality is the result of a complex relationship between ground sampling distance (GSD), modulation transfer function (MTF) and SNR. The combination of these estimates enables to indicate the quality and the amount of information that can be extracted from imagery. Leachtenauer *et al.* (1997) [RD19] define the general imagery quality equation (GIQE) where the interpretability of an image, expressed as the NIIRS (national imagery interpretability rating scale), is given by

$$\text{NIIRS} = 10.251 - a \log_{10} \text{GSD}_{GM} + b \log_{10} \text{RER}_{GM} - 0.656\ H_{GM} - 0.344\ \text{G/SNR} \tag{Eq. 51}$$

where:

- GSD_{GM} is the geometric mean of the ground sampled distance,

- RER_{GM} is the geometric mean of the relative edge response,

- H_{GM} is the geometric mean-height overshoot caused by the MTFC (MTF compensation),

- G is the noise gain associated with MTFC,

- in the current form of the GIQE, *SNR* is estimated for differential radiance levels from Lambertian scenes with reflectances of 7% and 15% with the noise estimated from photon, detector, and uniformity noise terms,

- if the *RER* exceeds 0.9, then *a* equals 3.32 and *b* equals 1.559; otherwise, *a* equals 3.16 and *b* equals 2.817.

The assessment of the MTF has been recognized as depending on the SNR (Delvit *et al.* 2003 [RD8]; Leloglu, Tunali 2006 [RD24]; Helder 2003 [RD13]). The MTF assessments are getting noisier as the SNR decreases.

In [RD4], Choi (2003) indicates that the SNR should be above 50 for accurate results with edge target methods. Helder and Choi (2005) [RD15] underline that significant tradeoff exists between MTF and SNR.

3.3.1 Minimum surface for SNR estimation

Reciprocally, it may be shown that the accurate assessment of the SNR is related to the PSF. SNR assessment requires accurate assessments of the standard deviation of the noise. Statistically, for typical remote sensing systems, the assessment of the standard deviation on an homogeneous surface needs a larger number of independent measures than the mean radiance assessment.

In other words, the minimum surface of homogeneous regions required for SNR assessment is typically larger than the one required for the mean radiance assessment. In the following, we establish a relation between the accuracy of the SNR assessment and the PSF.

The SNR assessment on a homogeneous surface can be viewed as the joint estimation of the mean m and the variance $v = \sigma^2$ of a random Gaussian white noise n. Let us call m_e, $v_e = \sigma_e^2$ and SNR_e respectively the estimation of m, $v = \sigma^2$ and $SNR = m/\sqrt{v} = m/\sigma$.

The aim of this section is to determine the minimum number N of independent measures of the random gaussian white noise n to obtain a good accuracy of the SNR assessment. In the remote imagery domain, this minimum number N is related to a minimum homogenous surface of $N\,\mathrm{GSD}^2$.

Let consider $\left\{ n_k \right\}_{k \in [1,N]}$ N independent measures of a random Gaussian white noise n whose mean m and variance $v = \sigma^2$ are both unknown. The unbiased optimal estimators m_e and v_e are, in this case:

$$m_e = \frac{1}{N}\sum_{k=1}^{N} n_k \qquad\qquad\text{(Eq. 52)}$$

and

$$v_e = \frac{1}{N-1}\sum_{k=1}^{N}\left(n_k - m_e \right)^2 \qquad\qquad\text{(Eq. 53)}$$

The SNR estimation SNR_e is then defined by:

$$SNR_e = \frac{m_e}{\sqrt{v_e}} = \frac{m_e}{\sigma_e} \qquad\qquad\text{(Eq. 54)}$$

3.3.2 Relative error of the mean estimator

From Student t-distribution T_{N-1} with N-1 degrees of freedom, the 95 % confidence interval (noted 95 %-CI) relative error of the mean estimator $\varepsilon_m^{0.95}$ can be derived:

$$\varepsilon_m^{0.95}(N) = \frac{t_{N-1}^{0.025}}{\sqrt{N}} \frac{\sigma_e}{m} \underset{N>30}{\approx} \frac{2}{SNR\sqrt{N}} \tag{Eq. 55}$$

where t_N^α is defined as $P\left(T_{N-1} > t_{N-1}^\alpha\right) = 1 - \alpha$ where *P* is the probability density function.

The relative error of the mean estimator depends on the number *N* of independent measures but also on the SNR. Most spaceborne imagery systems have a SNR greater than, let say, 50. Therefore, as illustrated by the figure 12, the relative error of the mean estimator is better than 0.4 % as long as the surface of the homogeneous region exceeds 10x10 pixel.
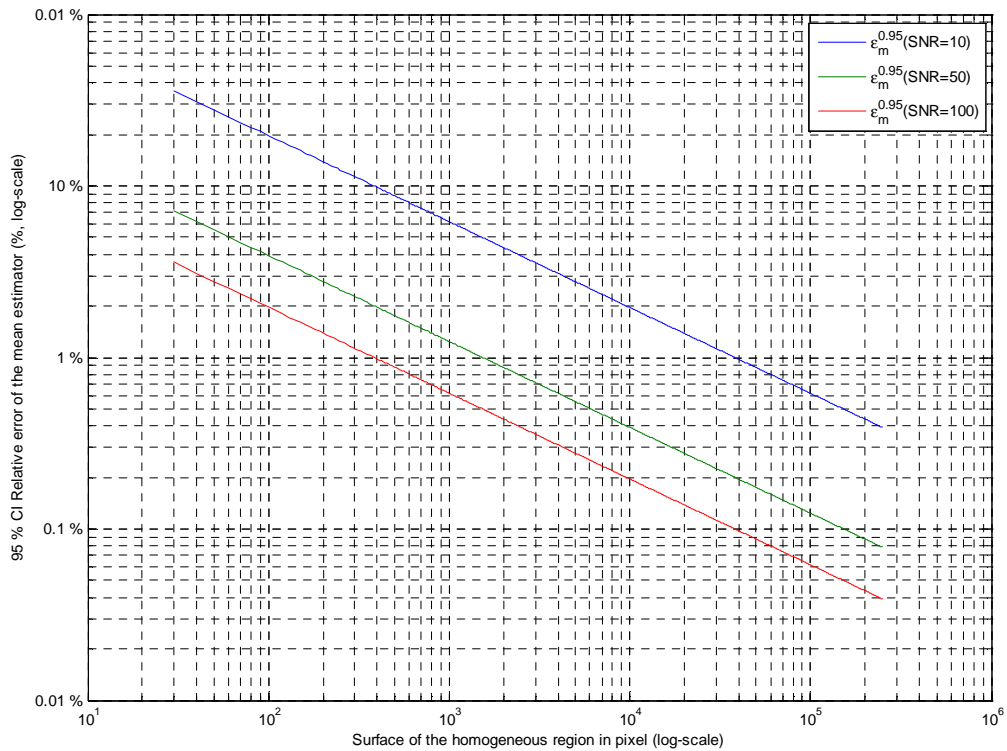

Figure 12: 95 %-CI relative error of the mean estimator versus surface of the homogeneous region in pixel, for three different SNR.

3.3.3 Relative error of the standard deviation estimator

From χ^2-distribution with N-1 degrees of freedom, the 95 % confidence interval relative error of the standard deviation $\varepsilon_\sigma^{0.95}$ can be derived:

$$\varepsilon_\sigma^{0.95}(N) \approx 1 - \frac{\sqrt{\chi_{N-1,0.025}^2}}{\sqrt{N}} \tag{Eq. 56}$$

where $\chi^2_{N,\alpha}$ is the inverse of the chi-square cumulative distribution function with *N* degrees of freedom at the values in α.

One can note that the relative error does not depend on the SNR: it only depends on the number *N* of the independent measures available. Also of interest is the fact that the relative error of the standard deviation estimator is more than 30 times greater than the relative error of the mean estimator for the same surface, for SNR greater than 50. As illustrated in figure 13, a relative error better than 1 % requires a surface of the homogeneous region greater than 140x140 pixels.
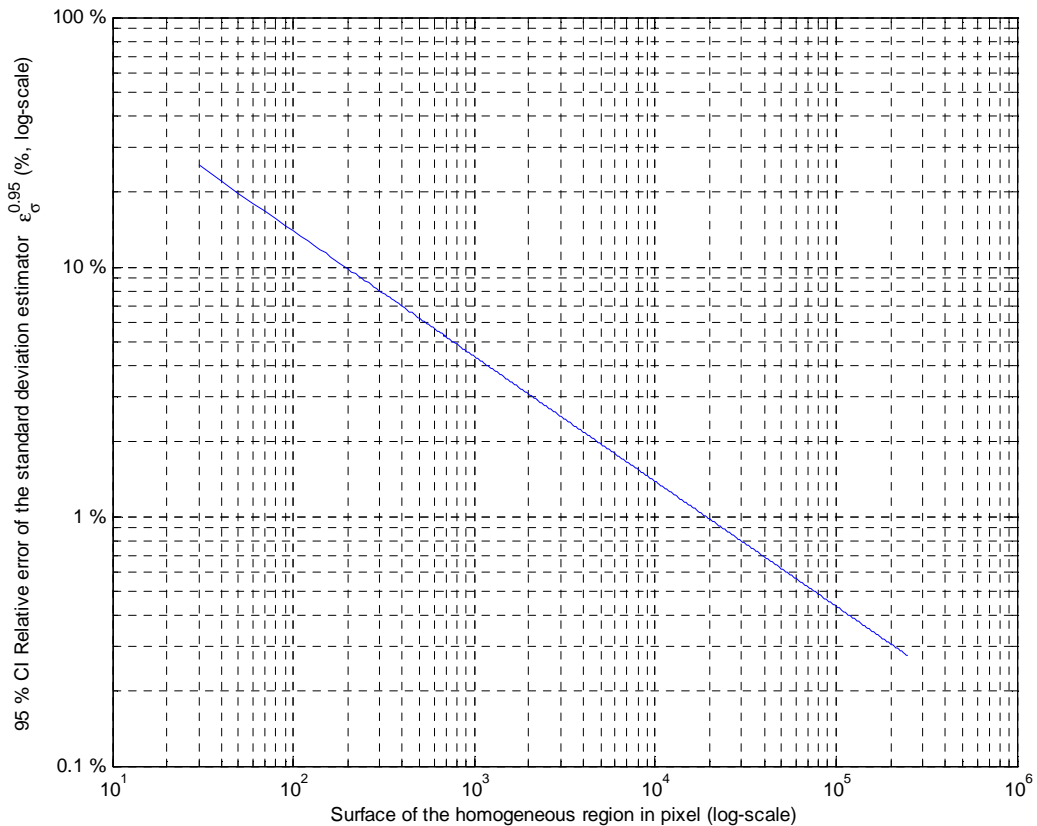

Figure 13:   95 %-CI relative error of the standard deviation estimator versus surface of the homogeneous region in pixel.

3.3.4 Relative error of the SNR estimator

For small mean and standard deviation estimation errors, dm and $d\sigma$, the corresponding SNR estimation error is given by:

$$dSNR = \frac{1}{\sigma}dm - \frac{m}{\sigma^2}d\sigma \qquad \text{(Eq. 57)}$$

Thus, the relative error *dSNR/SNR* can be written as:

$$\frac{dSNR}{SNR} = \frac{1}{SNR}\left(\frac{m}{\sigma}\frac{dm}{m} - \frac{m}{\sigma}\frac{d\sigma}{\sigma}\right)$$
$$= \frac{dm}{m} - \frac{d\sigma}{\sigma} \qquad \text{(Eq. 58)}$$

Then,

$$\varepsilon_{SNR}^{0.95} \approx \varepsilon_m^{0.95} \oplus \varepsilon_\sigma^{0.95} \underset{SNR>50}{\approx} \varepsilon_\sigma^{0.95}$$

(Eq. 59)

In other words, for typical space borne imagery system (SNR > 50), the 95 %-CI relative error of the SNR estimator is close to the 95 %-CI relative error of the standard deviation estimator. figure 14 displays the 95 %-CI relative error of the SNR estimator.
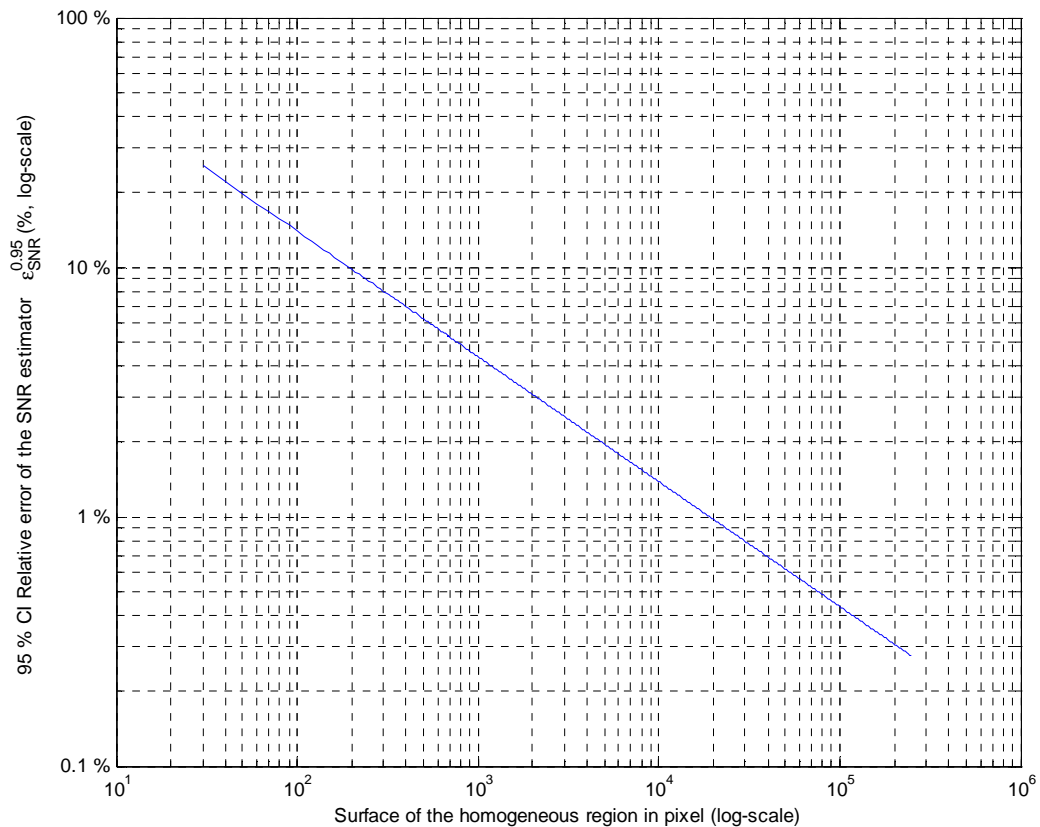

Figure 14: 95 %-CI relative error of the SNR estimator versus surface of the homogeneous region in pixel (SNR > 50).

3.3.5 Minimum surface and PSF extent

figure 14 gives the required minimum surface for a given relative SNR accuracy. However, the SNR assessment should take into account the spatial quality of the imaging system. The extent of the PSF gives the minimum distance between the homogeneous region and the surrounding background to avoid surrounding "contaminations" on the standard deviation assessment.

Consequently, given a relative SNR accuracy, the minimum homogeneous surface for SNR assessment, and more exactly for the assessment of the standard deviation, should obey these two constraints depicted in figure 15.

- L_T should be greater than the radius extent of the PSF;

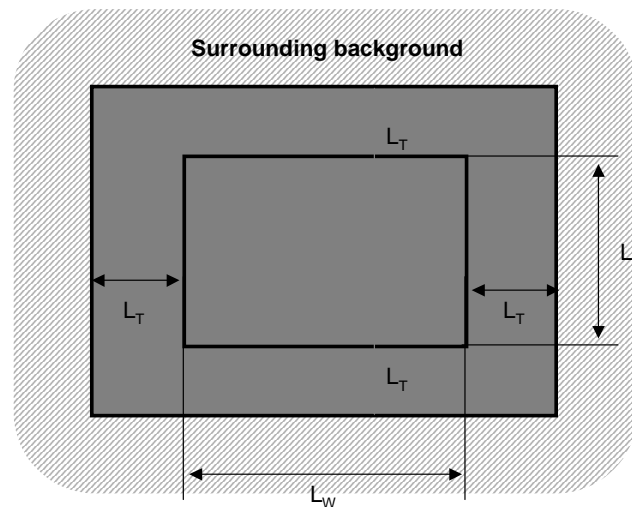- $L_H \times L_W$ should be greater than the required minimum surface.

Figure 15:   Homogeneous region for SNR assessment.

3.4   Methods to assess the SNR

A method for assessing the SNR is made up of three components that are linked: the selection of the site, the method to compute the mean *m* and the noise *σ*, and the instant when to apply the assessment with respect to routine operations and other calibration operations.

There are two approaches in the selection of a site: single view or synthetic landscape. In the single view approach, one image is acquired over a given site. In the synthetic landscape approach, several images are acquired and merged in order to create a synthetic landscape having the requested properties.

3.4.1 Single view – Homogeneous area

The principle of the single view for assessing the SNR is to find a homogeneous area representing a uniform landscape, to compute both the mean and the standard-deviation on this area and finally to build the ratio of the mean to the standard-deviation.

Homogeneous areas have been identified in the world and are used in various calibration operation. However, according to the various publications, it appears that the selection of a large homogeneous area is a problem. There is only a few sites, *e.g.*, Railroad Valley (Nevada, USA) (Biggar *et al.* 1991 [RD3]) or White Sands (New Mexico, USA), that may be suitable but their spatial homogeneity is not large enough (Henry and Meygret 2001 [RD16]; Marham *et al.* 1990 [RD25]; Thome *et al.* 2004 [RD39]).

Of course, the influence of the heterogeneity on the SNR assessment depends on the characteristics of the system. What is important are the scales of the heterogeneities with respect to the GSD. For a given intensity in heterogeneity, the larger the GSD, the smaller the influence is. The previous section shows that assessing the SNR for a large pixel size requests more ground surface than for a smaller pixel size. Thus, calibration sites may be suitable for certain systems and not for others.

The mean value of the radiance of the landscape should be large enough to obtain a reliable assessment of the SNR. This prevents deep oceanic areas to be exploited to that goal because their reflectivity is low, outside sun glitter conditions.

It appears from the literature survey that selecting a homogeneous area and quantifying its homogeneity is not an easy task. Accordingly, authors have adopted different approaches to cope with this problem of homogeneity. Many of these works intend to select landscapes with no or little high frequencies and to suppress the low frequencies (also called background) in order to obtain a homogeneous landscape.

3.4.2 Single view – Quasi-homogeneous area

One of the most known methods is the Fourier transform of a portion of an image (Jenkins and Watts, 1969 [RD17]; Oppenheim and Schafer, 1975 [RD28]). The noise appears at high wavenumbers (high frequencies). However, the very chaotic behavior of the spectral density for high wavenumbers as well as the presence of large scale trends may render the estimates of both the noise σ and the mean m rather inaccurate.

A more recent method is to exploit the variogram γ, also called structure function in turbulence (Panchev, 1971 [RD29]). Because the variance of the noise appears in the variogram as the nugget variance, variogram offer a good readiness of the noise variance even in presence of large variations of the actual signal. It is also invariant, by definition, to systematic errors.

The variogram depicts the spatial variability at increasing distances h (scales) between sample points (Matheron, 1963 [RD26]):

$$\gamma(h) = E((Z(x+h)-Z(x))^2) \hspace{3cm} \text{(Eq. 60)}$$

where E is the mean operator.

This quantity divided by two is called the semivariogram. The variogram puts on a rational and numerical basis the well-known concept of the "range of influence" of the variable in a fashion more or less similar to the covariance function for a stationary function. Figure 7 illustrates a semivariogram in presence of uncorrelated noise. As the distance h increases, the semivariogram tends to the variance of the image.
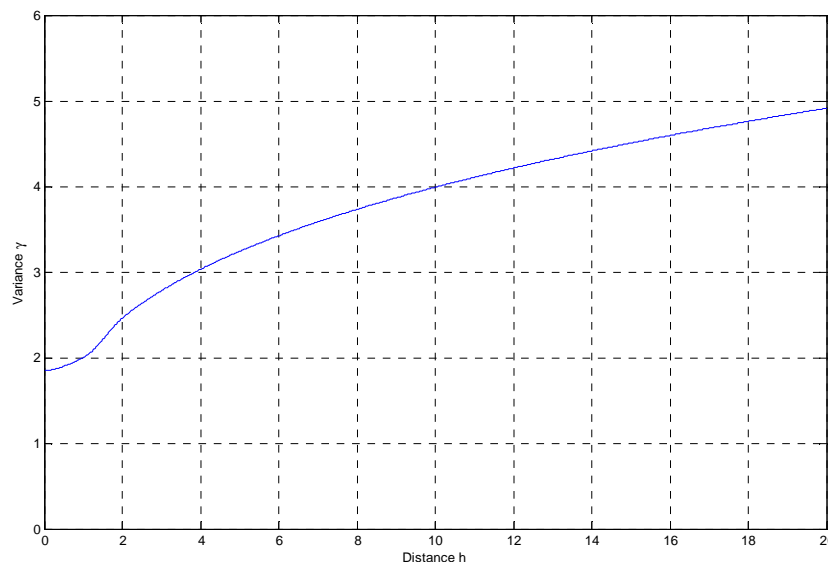

Figure 16:   Illustration of a semivariogram with uncorrelated noise.

The variogram should equal 0 as h tends to 0. The value of $\gamma(h)$ close to origin gives a measure of the variance of the structures the sizes of which are smaller than the sampling

size. This variance $\gamma(0)/2$ is called the nugget effect or nugget variance or random variance.

The spatial behavior of Z(x) is closely related to the shape of $\gamma(h)$ near the origin. If $\gamma(h)$ is twice differentiable it the origin, then Z(x) is smoothly continuous and it contains rather energetic long wavelength terms. If $\gamma(h)$ is linear near the origin, then Z(x) is continuous but not necessarily derivable. If $\gamma(h)$ is not continuous at the origin, hence presenting a nugget effect, Z(x) is not continuous and is rather erratic.

In presence of uncorrelated noise, and if $\gamma_{true}(h)$ denotes the actual variogram without noise, one obtains:

$$\gamma(h) = \gamma_{true}(h) + 2\,\sigma \qquad\qquad\qquad \text{(Eq. 61)}$$

The nugget effect $\gamma(0)$ is the variance of the noise σ. If the area is homogeneous, the spatial average of the radiance provides the mean m. If heterogeneous, the image may be locally detrended by adjusting e.g., a polynomial function. The residuals are considered as stationary; the variogram and the average may be computed.

Curran and Dungan (1989) [RD6] and Wald (1989) [RD43] assessed the SNR for respectively AVIRIS and AVHRR images by this means. Outside the difficulties in detrending properly, the issue is the estimation of the unknown $\gamma(0)$ from some estimated values of $\gamma(h)$. If one assumes that $\gamma(0)$ and $\gamma(1)$ are equal, one may overestimate the variance of the noise. Other approaches, such as extrapolation to ordinate using analytical forms of the semivariogram, may lead to underestimation.

In a recent work [RD12], Guo and Dou (2008) propose a common and feasible way for estimating the variance of the noise, provided a suitable sub-image is found where the signal may be assumed to be stationary; the first application to FY-2 thermal imagery is convincing.

In studies on signal denoising presented in [RD9], Donoho and Johnston (1994) compute the wavelet coefficients of quasi-homogeneous areas. These wavelet coefficients represent the local intensity of structures for a given scale. Taking the *median* absolute deviations noted MAD of the wavelet coefficients, Donoho and Johnston (1994) [RD9] find that the standard-deviation of the noise can be estimated in a very robust way by:

$$\sigma = MAD / 0.6745 \qquad\qquad\qquad \text{(Eq. 62)}$$

This method can also be applied in an area exhibiting smooth low frequencies; detrending is nevertheless necessary for the computation of the mean.

More recently, Delvit *et al.* (2003) in [RD8] and [RD7] exploit both the wavelet transform and the variogram to compute the SNR. They stress the importance of the characterization of the landscape in order to discriminate the landscape information from the noise. They choose to model the semivariogram of an image by the following function:

$$\gamma(h) = e^c\, h^b\, e^{a\,\ln(h)} \qquad\qquad\qquad \text{(Eq. 63)}$$

where *a*, *b*, and *c* are parameters to be determined, called the landscape structure parameters.

The proposed method is based on an artificial neural network (ANN). The principle is to firstly train the ANN for the noise of simulated or perfectly known images, and then to use the ANN to assess the noise of unknown images. Inputs to the ANN are the landscape structure parameters and elements that characterize the energy in high frequencies. The

authors choose the wavelet packets decomposition, focusing on those packets whose noise is prominent against the landscape signal on account of the damping of the MTF.

More precisely, as illustrated by the figure 17, MTF induces very important damping in the diagonals of the Fourier space. For those Fourier areas, the landscape contribution is the image can be negligated.
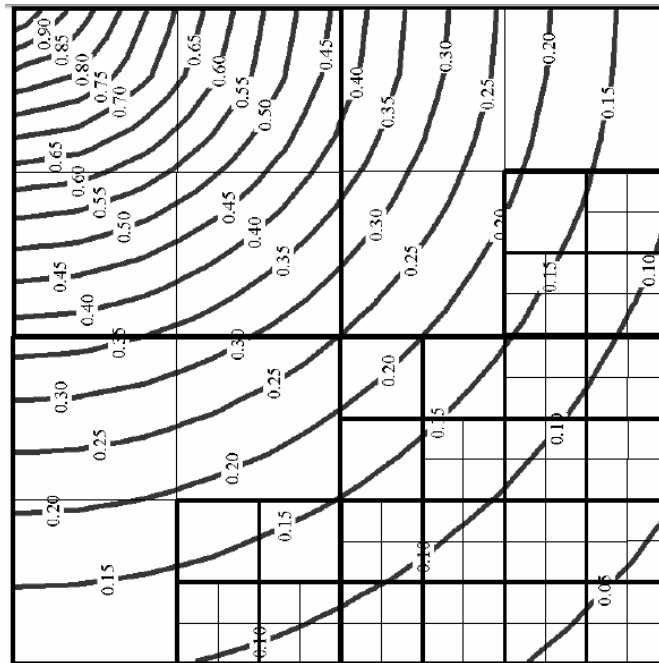

Figure 17:   Example of adapted wavelet packets decomposition to isolate wavelet coefficients where the MTF is low (source: [RD8]).

The entropy and the L² norm of the packet are the inputs to the ANN. This method has also a similar component devoted to the assessment of the MTF; it is quite promising. Its qualities should be demonstrated in real cases. Though the authors claim that it should work for any type of landscape, it is believed that images exhibiting smooth landscapes with low-energy intrinsic high frequencies would be more suitable for SNR assessment.

3.4.3 Synthetic landscape

The constraint on a homogeneous existing area may be reduced if one considers a synthetic landscape. A synthetic landscape is constructed by the fusion of actual single images (Wald, 1999 [RD45]): the properties of the synthetic landscape are more suitable to SNR assessment than those of each single image.

One possible solution is to exploit the existence of desert area whose reflectance is very stable in time, once corrected for bi-directional effects. Such areas were identified by Cosnefroy *et al.* (1996) [RD5] in Northern Africa.

These sites are exploited by Eumetsat for the calibration of the Meteosat satellites (Govaerts 1999 [RD10]; Govaerts *et al.* 1998 [RD11]) VEGETATION (Henry, Meygret 2001 [RD16]) and SPOT5 (Lebègue *et al.* 2003 [RD20]).

If the same pixel is acquired at different cloud-free instants, a time-series of radiances may be constructed which should be constant. The mean and standard-deviation may be computed and the SNR assessed at this radiance level. This approach has not yet been exploited. However, a fairly close approach is used for SPOT5 for the column-wise noise (Lebègue *et al.* 2003 [RD20]). Snowy expanses of Greenland (in boreal summer) and

Antarctic (in austral summer) are assumed to be constant in time, at least between two consecutive passes. If the two images are perfectly superimposed, the landscape contribution at any scale can be eliminated by a simple difference at each pixel for the area of interest. The residuals are the noise. The standard-deviation is then computed from the residuals, the mean radiance is estimated from the mean of the two images and the SNR can be estimated.

A parameterized model of column-wise SNR function of radiance provides the SNR value at the reference radiance L_2:

$$SNR = \frac{L_2}{\sqrt{\rho L_2 + v_0}}$$ (Eq. 64)

where:

- ρL_2 is the variance of the photonic noise, proportional to the considered entrance radiance;

- v_0 is the variance of the readout noise independent of the photonic noise

Another possible solution is to construct this landscape by summing up cloudy images. After a certain period, all pixels are cloudy and under certain conditions, this synthetic landscape may be considered as uniform.

The principle has been discussed by Vermote and Kaufman (1995) in [RD40] for absolute calibration. Under certain conditions, radiance reflected by thick clouds exhibits low spatial variance (Sèze, Desbois 1987 [RD35]; Sèze, Rossow 1991 [RD36]). If one is able to pick-up such cloudy pixels and only those, one may construct a synthetic image of high radiance and low variance. This approach has not been tested for SNR assessment. For past experience, it should be recommended to focus on clouds over deep oceanic areas (*e.g.*, southern hemisphere) to prevent any influence of the ground whose reflectance often exhibits marked spectral changes, and to avoid specular reflection at the surface of the ocean, which is marked by large gradients in reflectance (Wald, Monget 1983 [RD42]).

Such an approach has been applied for performing inter-band calibration of POLDER (Asmami, Wald 1993a [RD2]) or AVHRR (Asmami, Wald 1993b [RD1]; Wald 1998 [RD44]) but for single images. These authors underline that cloud selection is crucial for accurate results and that it depends upon the wavelength under concern. For AVHRR, where the spectral bands are large, the method does not call upon very bright clouds. On the contrary, clouds with medium reflectivity are an ideal target. The method constructs the density of probability of the cloudy pixels and imposes constraints in representation of clouds of medium brightness.

In [RD21], Lefèvre *et al.* (2000) devised a method for absolute calibration of Meteosat images that was successfully applied by Rigollier *et al.* (2002) [RD34] for the calibration of several years of images. This method may be applied to the assessment of the SNR.

Lefèvre *et al.* [RD21] found two statistical quantities in Meteosat images that are constant with time. They state that this constancy is due to the fact that in the entire field of view of the Meteosat sensor, the mixed presence of land, ocean, and clouds of different reflectivity over approximately one third of the Earth, whatever the day and time of the year, may lead to the preservation of such statistical quantities with time.

If $L_5(t)$ and $L_{80}(t)$ denote respectively the radiances corresponding to the percentiles respectively 5 % and 80 % of the histogram of radiances of the mid-day image, they found that

$$\frac{\partial}{\partial t}\left(\frac{L_{80}(t) - L_5(t)}{I_0(t)}\right) = 0 \qquad \text{(Eq. 65)}$$

i.e., the quantity *$(L_{80}(t) - L_5(t)) / I_0(t)$* is constant over time, where *$I_0(t)$* is the incoming extraterrestrial irradiance. If δ is the relative eccentricity correction characterizing the change with time in the distance between the sun and the earth, then

$$I_0(t) = I_0 (1+\delta) \qquad \text{(Eq. 66)}$$

Using several images, one may construct a time series of this quantity, *L_5,* and *L_{80}*. Then, one may compute the mean value *m*

$$m = E [(L_{80} + L_5) / 2 \qquad \text{(Eq. 67)}$$

and the noise σ:

$$\sigma^2 \approx \text{var}[(L_{80} - L_5) (1 - \delta)] \qquad \text{(Eq. 68)}$$

where *var* denotes the operator of variance.

This approach may be applied to sensors having a narrow field-of-view. In that case, several images of *e.g.,* southern oceans with clouds should be summed up to find a constant statistical quantity.